Highly Efficient Passive Thermal Micro-Actuator

Harald Steiner, Franz Keplinger, Johannes Schalko, Wilfried Hortschitz, and Michael Stifter

Abstract—A passive thermal micro-actuator with large area specific work and large displacement, fabricated of electroplated nickel on a silicon substrate is presented. The actuation relies on the thermal expansion of beams in a V-shaped geometry. Two V-shaped beam stacks are aligned opposite to each other and are coupled to a lever transmission. The actuator exhibits low energy losses due to the deformation of the structure and can efficiently convert the thermally induced elastic energy into mechanical work. An analytical model considers these thermally induced mechanical energies and the energy losses caused by the deformation of the material. The calculated deflections are compared with the measured ones and results of finite-element method simulations. The presented actuator operates completely passive, relies only on temperature changes of the surrounding environment, and exhibits a measured temperature-dependent linear deflection coefficient of 1.48 μm/K with a simulated blocking force of 57 μN/K. The structure occupies an area of 2135 × 1831 μm^2 and the area specific work is calculated to be 21.7 μJ/K^2/m^2, beating state of the art thermal actuators. As proof-of-concept, a passive micro-electro-mechanical systems temperature threshold sensor is fabricated, featuring the actuator and a bistable beam that switches between two stable positions when a specific threshold temperature is exceeded. [2014-0317]

Index Terms—Micro mechanical system, passive thermal actuator, V-shaped, electroplated nickel, energy efficient.

I. INTRODUCTION

THERMAL actuators are key elements of many MEMS (micro-electro-mechanical systems) as micro grippers, latches, or switches [1]–[6] utilizing resistive heating elements [7]–[11]. An often used actuator design is the V-shaped beam, also known as the "chevron type" thermal actuator [12]–[15]. Such components are commonly heated up to several hundred degree Celsius via Joule heating, as their displacement coefficients between 0.01 μm/K and 0.5 μm/K are rather low. Thus, they exhibit high losses of thermal energy and an inefficient conversion of input heating energy into mechanical output work. For applications where feasible temperature differences are limited, such devices have insufficient

H. Steiner, W. Hortschitz, and M. Stifter are with the Center for Integrated Sensor Systems, Danube University Krems, Krems an der Donau 3500, Austria (e-mail: harald.steiner@donau-uni.ac.at; wilfried.hortschitz@donau-uni.ac.at; michael.stifter@donau-uni.ac.at).

F. Keplinger and J. Schalko are with the Institute of Sensor and Actuator Systems, Vienna University of Technology, Vienna 1040, Austria (e-mail: franz.keplinger@tuwien.ac.at; johannes.schalko@tuwien.ac.at).

Color versions of one or more of the figures in this paper are available online at http://ieeexplore.ieee.org.

Digital Object Identifier 10.1109/JMEMS.2015.2457094

displacement coefficients and their energy losses are too large. For instance, when a MEMS switch should be operated by such an actuator and the electrical power and the available temperature change is limited. Hence, a thermal actuator design aiming at temperature displacement coefficients of more than 1 μm/K was developed. Great effort was allocated to achieve an efficient conversion of thermally induced elastic energy into mechanical performance (sec. II). Furthermore, the presented actuator can operate completely passive, only relying on the temperature change of the surrounding environment. Since common analytical models for such actuators are relatively complex and can be solved only semi-analytically [16]–[21], a simplified analytical model is presented in sec. III. Its closed form reveals directly all relevant parameters for the design of the actuator. Section IV explains the manufacturing process used and sec. V reveals the performed computer numerical simulations. Experimental investigation and their results are discussed in sec. VI and sec. VII. Furthermore, a proof-of-concept is presented in sec. VII, where the actuator is combined with a bistable beam, establishing a passive temperature threshold sensor. Since the storage and transportation temperatures of refrigerator cargo or blood transfusion bags in clinical usage is critical, such a sensor is of advantage to ensure a proper cooling chain [22], [23]. The actuator itself is designed to be operated in a temperature range from −50 °C up to +100 °C. This range is determined and limited by the occurring mechanical stress due to the deformation of the structure. Finally, the paper is summarized in a conclusion in section VIII.

II. DESIGN

The presented actuator design relies on V-shaped ("chevron type") beams. Two packs of six 800 μm long beams in parallel with a tilting angle of $\gamma = 4°$ form one half of the actuator stack (Fig. 1). This beam stack has a mirrored counterpart which is shifted along the mirror axis (symmetry *A*). Both stacks are connected via coupling bars to a lever that moves in-plane depending on the change in temperature. The movable structure is fixed to a Si-substrate at four anchor regions at the corners of the structure. Mechanical stress energy is accumulated within the V-shaped beams due to differences in the thermal expansion of the active structure material (Ni), the substrate (Si), and temperature changes of the surrounding environment. A single clamped cantilever releases this stress by axial elongation. For the V-shaped design, however, a deflection in the y-direction is preferred. This buckling introduces an elastic energy within the individual beams. When the stack deflects in y-direction, an additional elastic deformation energy is induced within the
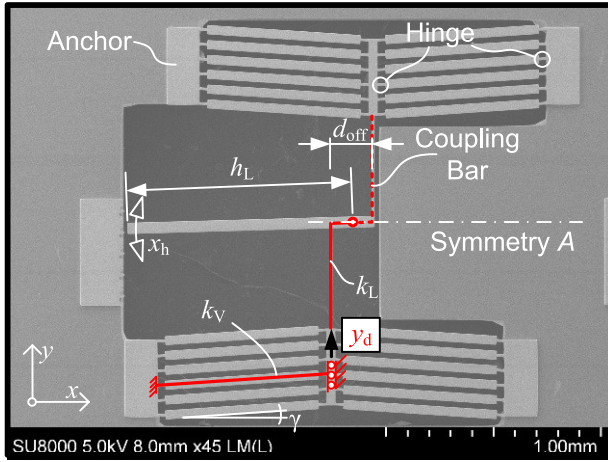
Fig. 1. Scanning electron micrograph of the thermal actuator. Two mirrored V-shaped beam stacks are connected to a lever beam. For the analytical model, the structure is separated into V-shaped beam stacks and a lever transmission with the spring stiffnesses k_V, k_L, respectively.

TABLE I

GEOMETRY PARAMETERS OF THE STRUCTURE. COMPARE FIG. 1 AND FIG. 2 FOR THE INDIVIDUAL VARIABLES

V-shaped Beam		Lever Transmission	
l_1	$40\,\mu m$	l_3	$475\,\mu m$
l_2	$361\,\mu m$	l_4	$100\,\mu m$
b_1	$10\,\mu m$	b_3	$10\,\mu m$
b_2	$40\,\mu m$	b_4	$50\,\mu m$
γ	$4°$	h_L	$1105\,\mu m$
n	6		
I_1	$1250\,\mu m^4$	I_3	$1250\,\mu m^4$
I_2	$80000\,\mu m^4$	I_4	$156250\,\mu m^4$
A_1	$150\,\mu m^2$	A_3	$150\,\mu m^2$
A_2	$600\,\mu m^2$	A_4	$750\,\mu m^2$

coupling bars. The system is in thermodynamic equilibrium when the overall energy is minimal and, therefore, an equilibrium of forces is established. A sort of hinge is formed by short flat springs in order to reduce the deformation energy of each V-shaped beam. These hinges have a width of 10 μm, whereas the rest of the V-shaped beam is 40 μm in width. The coupling bars are 475 μm in length and feature also a width of 10 μm. The offset d_{off} between the beam stacks amounts 200 μm, and the lever exhibits a length of $h_L = 1105$ μm with a width of 50 μm. The structure is 15 μm in height and consists of electroplated Ni on a Si-substrate. Table I lists all geometric parameters, where the individual variables can be found in detail in Fig. 1 and Figure 2. The actuator is designed for passive operation in a temperature range from -50 °C up to $+100$ °C, only relying on temperature changes of the surrounding environment.

III. ANALYTICAL MODEL

The geometry is separated into the V-shaped beam stacks and the lever transmission for the analytical model. The spring stiffnesses k_V and k_L of a single beam of the stack and the lever transmission, respectively, are calculated for a given deflection y_d (Fig. 1). Finally, an equilibrium of the total
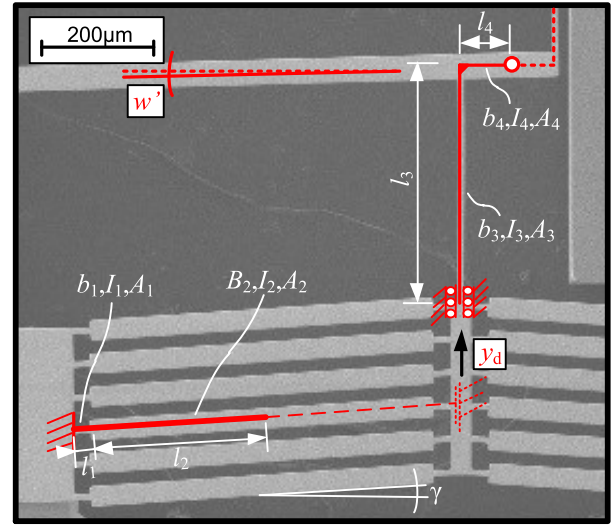

Fig. 2. Detailed view on the different lengths, beam properties, and boundary conditions for calculating the spring stiffnesses.

energy due to the thermally induced expansion and the elastic energy of the deflected structure leads to the temperature dependent deflection at the tip of the lever x_h (actuator stroke).

A. Deflection

The spring stiffnesses k_V and k_L as depicted in Fig. 1 are calculated in accordance to the static Euler-Bernoulli beam theory to be

$$k_V = \frac{E}{\frac{l_1 l_2}{I_1}(l_2 + l_1) + \frac{1}{3}\left(\frac{l_2^3}{I_2} + \frac{l_1^3}{I_1}\right)} \qquad (1)$$

and

$$k_L = \frac{E\left(3\frac{I_3}{l_3^3} + \frac{A_4}{l_4}\right)}{\frac{I_3}{I_4}\frac{l_4^3}{l_3^3} + \frac{A_4}{I_4}\frac{l_4^2}{3} + \frac{3l_4^2}{l_3^2} + \frac{A_4}{I_3}\frac{l_3 l_4}{4} + \frac{I_3}{A_3}\frac{3}{l_3^2} + \frac{3A_4}{2A_3}\frac{l_3}{l_4}} \qquad (2)$$

where E is the Young's modulus, $I_{1,2,3,4}$ are the second moments of area, $A_{1,2,3,4}$ are the cross sectional areas, and $l_{1,2,3,4}$ are the lengths of the individual beam sections (compare Fig. 2). The deflection of the tip of the lever x_h in dependency of the deflection y_d can be calculated with the length of the lever h_L and the inclination w', resulting from solving the static Euler-Bernoulli beam theory, to be

$$x_h(y_d) = \left[\left(\frac{l_4^2}{6I_4} - \frac{l_3}{l_4 A_3}\right)\frac{k_L}{E} + \frac{1}{l_4}\right] \cdot y_d \cdot h_L. \qquad (3)$$

The energy equilibrium of the thermally induced elastic energy and the deformation energy of the structure is calculated to derive the temperature difference dependent deflection of the tip of the lever. The thermally induced elastic energy in the two mirrored stacks is approximated with the true strain by

$$U_T(y_d) = 2 \cdot n \int_0^{\bar{y}_d} \ln\left(\frac{l_2 + \sin(\gamma)y_d}{\exp(\alpha \Delta T) \cdot l_2}\right) E A_2 dy_d, \qquad (4)$$

where n is the number of parallel beams, α the coefficient of thermal expansion (CTE), ΔT the temperature change, and γ the angle of the V-shaped beam. It is assumed, that the temperature is homogeneously distributed over the whole device and the temperature change of the surrounding environment leads again to a quasi-static homogeneous temperature distribution. Since the length of the hinge l_1 is small compared to l_2 it is neglected further on. The deformation energy of the structure is given by the individual spring stiffnesses and yields

$$U_D(y_d) = (2n \cdot k_V + k_L) \frac{y_d^2}{2}. \qquad (5)$$

When the energy minimum of $\frac{d(U_T + U_D)}{dy_d} = 0$ is calculated and a Taylor approximation for $\sin(\gamma) \frac{y_d}{2} \ll 1$ up to $\mathcal{O}\left((\sin(\gamma) \frac{y_d}{2})^2\right)$ is applied, the corresponding deflection yields

$$y_d = \frac{2 \cdot l_0 \cdot \alpha \Delta T}{\sin(\gamma) + \frac{2l_0}{E \cdot A_2} k_{comp}}, \qquad (6)$$

with $l_0 = l_1 + l_2$ and $k_{comp} = k_V + \frac{k_L}{2n}$. The dependence of the angle γ with the deflection y_d has to be taken into account and the differential form of Eq. 6 results

$$dy_d = \frac{2 \cdot l_0 \cdot \alpha \, dT}{\sin(\gamma + d\gamma) + \frac{2l_0}{E \cdot A_2} k_{comp}}, \qquad (7)$$

with the differential angle

$$d\gamma = \arctan\left(\frac{l_0 \cdot \tan(\gamma) + dy_d}{l_0}\right) - \gamma. \qquad (8)$$

A Taylor approximation of the right hand side of Eq. 7 for $dy_d \ll 1$ leads to a quadratic equation with two solutions. Only the resulting physical relevant solution is taken into account, yielding for $\alpha dT \ll 1$ a total temperature dependent deflection of the V-shaped beam stack of

$$y_d(\Delta T) = \frac{2 \cdot l_0 \cdot \alpha \Delta T}{\sin(\gamma) + \frac{2l_0}{E \cdot A_2} k_{comp}}$$
$$- \frac{l_0 \cos(\gamma)^2 (\alpha \Delta T)^2}{\left(\sin(\gamma) + \frac{2l_0}{E \cdot A_2} k_{comp}\right)^3}. \qquad (9)$$

This deflection can now be used in Eq. 3 to calculated the stroke of the tip of the lever x_h.

B. Force

To prevent any movement of the tip, a blocking force has to be applied. This blocking force is equivalent to the maximal force that the actuator can apply for a specific temperature change. For this considerations, in-plane deformations of the lever are neglected since the lever is 50 μm in width and the second moment of area is much larger compared to that of the small hinges. Thus, the blocking force of the actual actuator can simply be attributed to the force F_V generated by the V-shaped stacks, occurring at the coupling bars:

$$F_V = E \frac{l_0 \alpha \Delta T}{\left(\frac{l_2}{A_2} + \frac{l_1}{A_1}\right)(1 + \alpha \Delta T)} \cdot \sin(\gamma) \qquad (10)$$

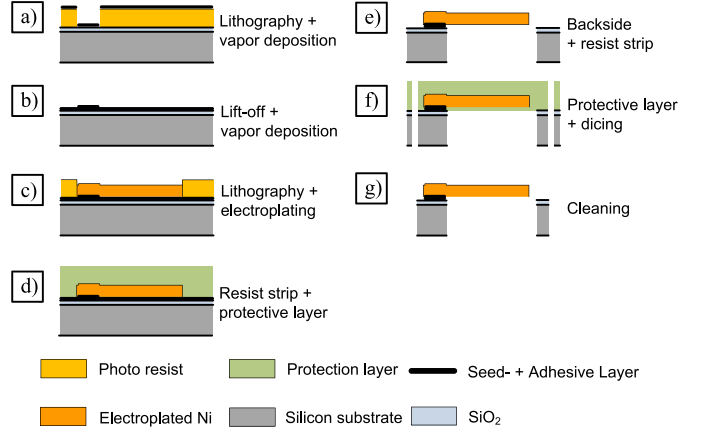$$F_{tip} = 2 \cdot n \cdot F_V \frac{l_4}{h_L}. \qquad (11)$$

Fig. 3. Schematic overview of the device fabrication. (a)-(c) After depositing the adhesive layer and the seed layer, Ni is electroplated. (d)-(e) A protective resist is coated and the substrate beneath the structures is removed by a DRIE to avoid any stiction problems. (f)-(g) Again a thick resist layer is spray coated to protect the structures during the dicing of the wafer. Afterwards, the individual dies are manually rinsed and cleaned.

This is the maximum value of the force that the actuator can apply when the movement of the tip of the lever is restricted.

IV. FABRICATION

A silicon (100) single crystal wafer with a 270 nm thick SiO$_2$ top layer is used as substrate.

Preparation: At first, photo resist (AZ5214, spun at 3150 rpm, hard bake 107 °C, 5 min, hot plate Sawatec) is deposited and patterned by photo lithography (SÜSS, MA150), to define anchor regions (Fig. 3a). In these areas, the Ni structures are fixed to the surface of the wafer with a 50 nm Cr adhesive layer and 200 nm Cu layer, both vapor deposited. After lift-off in acetone, a 2 nm thick Ti adhesive layer and a 300 nm Cu layer are vapor deposited all over the wafer surface (Fig. 3b). This Cu layer acts as seed layer for the electroplating process.

Galvanic: The photo resist AZ125nXT, compatible to the following galvanic process, is deposited in two layers (1000 rpm, 6 min at 120 °C on a hot plate, Sawatec) resulting in a thickness of 45 μm in total. It is exposed to UV-light (365 nm, SÜSS, MA150) for 40 s, and developed for 2 min with AZ628 MIF. The openings are filled with compact, pore free Ni with pulse reverse plating in a Nickel sulfamate electrolyte with 1.27 mol/l Ni (75 g/l Ni) at 40 °C (Fig. 3c) [24]. The pulse frequency is set to 80 Hz and the ratio cathodic/anodic pulse current density varies from 1 to 0.2 with a maximum applied current density of 110 A/m^2 . After electroplating of the 15 μm thick Ni layer, the resist is removed with Technistrip P1316 at 60 °C for 3 min. The wafer is rinsed afterwards with deionized-water (DI-water) and isopropanol and, afterwards, the surface is cleaned from residuals in an O$_2$ plasma (150 W, 6.7 Pa, 10 min).

Backside Etch: For the following backside etch, the topside is covered with a protective layer (resist AZ4562, Fig. 3d). This resist is spray coated three times with intermediate drying steps (5 min at 90 °C on a hot plate, Sawatec). The backside is coated two times with
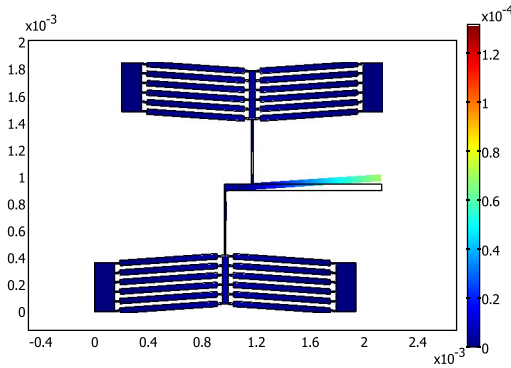
Fig. 4. Result of the FEM simulation, revealing the deformation of the structure due to changes in homogeneously distributed surface temperature. The plot shows the deflection of the structure at 0 °C, simulated with an effective CTE of $\alpha_{\text{eff}} = 11$ ppm/K and an intrinsic stress of $\sigma_{\text{ini}} = 170$ MPa.

TABLE II
GEOMETRY AND MATERIAL PARAMETERS OF THE
STRUCTURE AND THE FEM MODEL [25], [26]

FEM Parameters		
E	160 GPa	Young's modulus
α_{eff}	11 ppm/K	CTE
h	15 µm	Structure height
ρ	8900 kg/m³	Density
ν	0.33	Poisson's ratio

a photo resist (AZ6624, 3000 rpm). The first layer is dried for 5 min at 107 °C, and the second layer 3 min at 107 °C. It is exposed to UV light (365 nm for 40 s, EVG 620) and developed with AZ628 MIF. The backside etch of the silicon wafer is performed by a deep reactive ion etch (DRIE) process (Bosch-process, Oxford LF Yatton). The oxide under the structures is removed by a backside plasma etch step (10 min, 200 W, 20 Pa, $CHF_3 + O_2$). The substrate under the movable Ni structures is completely removed to avoid stiction problems. Afterwards, the top and bottom resist layers are removed in acetone and both sides of the wafer are cleaned with O_2 Plasma (150 W, 6.7 Pa, 10 min) to remove resist residuals (Fig. 3e).

Release: To release the structures, the Cu seed layer is etched with sodium persulfate for 6 min (Fig. 3e). Subsequently, the wafer is rinsed with DI-water, isopropanol and dried with N_2. Again, a protective overcoat (resist AZ4562) is applied on the topside by the spray coating process. The resist acts as protection and mechanical stabilization of the structures for the following dicing of the wafer (Fig. 3f). Finally, the individual dies are manually rinsed with acetone and isopropanol to remove the protection layer (Fig. 3g).

V. FINITE ELEMENT MODEL

The structure is modeled as a 3D shape in a finite element method simulation (FEM, COMSOL Multiphysics®[1]) in order to predict the characteristics of the thermal micro-actuator. The non-linear solid stress-strain model includes mechanical stresses introduced by thermal expansions of the material and
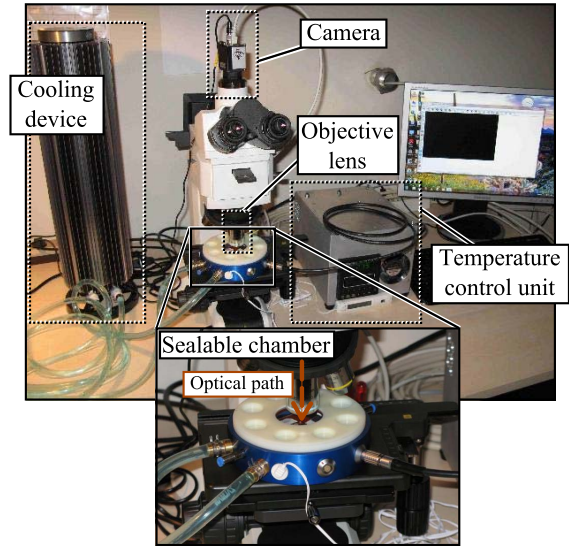
[1] www.comsol.com/comsol-multiphysics

Fig. 5. The test setup comprises a sealable chamber, a microscope with an objective lens with long working distance, a camera, a cooling device, a Peltier-element, and a temperature control unit.

intrinsic stresses due to the manufacturing process (Fig. 4). The material parameters employed are listed in Table II. The effective coefficient of thermal expansion (CTE) is the difference between the CTE of the actuator material and the CTE of the substrate material. The boundaries in the anchor regions are fixed and the rest is freely moveable. The deflection of the tip of the lever is evaluated at a number of temperatures, where the temperature is homogeneously distributed along the surface.

The intrinsic stress value at room temperature is evaluated by measuring the initial deformation of the structure in comparison to simulations at different stress levels. When the structures are manufactured and released from the backside, the intrinsic stress relaxes. The resulting deflection is measured with an optical microscope at room temperature. The stress is adapted in the FEM model and the resulting deflection is compared to the measured one, leading to an intrinsic stress of $\sigma_{\text{ini}} = 170$ MPa. The blocking force to be expected is evaluated by fixing the tip of the lever and simulation of the reaction forces at various temperatures.

VI. MEASUREMENT

A. In-Plane Deflection

A characterization setup is designed and built to measure the deflections of the tip of the lever at well defined temperatures. It consists of a sealable chamber with an optical inspection window, a Peltier-element supplied by a temperature control unit, a cooling device, and a microscope with a $50\times$ objective lens, featuring a long working distance (Fig. 5). The chamber is gas-tight to obtain reproducible environmental conditions even below the freezing point of H_2O. It is purged with N_2 to prevent any water condensation on cold surfaces. The two stage Peltier-element (Global Component Sourcing, ET2-196-19-14) with a PID temperature control unit allows for a controlled heat-up and cool-down of the test specimen between -30 °C up to $+40$ °C. The closed loop controller (Eurotherm 820) sets the current of the Peltier-element,
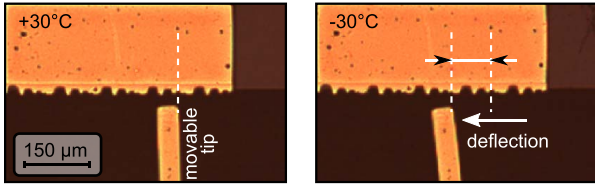
Fig. 6. Micrograph of the tip of the structure at different temperatures. The deflection is quantified by measuring the pixel shift of the moving lever.

whereas a Pt-100 resistance thermometer delivers the actual temperature input for the control loop. It is located on top of the Peltier-element, next to the test specimen. The bottom side of the Peltier-element is held at room temperature with a commercial water cooling device. The chamber features an total height of only 3.5 cm to fit under the microscope (Nikon Eclipse LV150, CFI L Plan Epi SLWD 50X).

The chamber is loaded with the test die, closed, and purged with N_2 for 1 min to remove residual humidity. The test specimen is located on top of the Peltier-element and thermally connected with a thermal conductive paste, where the size of the specimen and the contact area is 8×8 mm^2. Since the thermal conductivity of the Si is high compared to the surrounding N_2 atmosphere and, therefore, the convective and conductive cooling is negligible, it can be assumed that the device has the same temperature as the surface of the Peltier-element, which is further on referred to as environmental temperature. This temperature is varied in 10 °C steps between +40 °C to −30 °C. After setting the individual temperature values a dwell time of 30 seconds is waited before an image is taken (camera system IDS GigE μEye SE, 100 fps). This ensures that the Peltier-element has reached the set temperature and a homogenous temperature distribution on the topside of the structure has been established. The excitation of the tip of the structure is measured by calculating the pixel shift of the tip of the structure between two images (Fig. 6). The camera system in combination with the microscope and the objective exhibits a calculated resolution of 220 nm/px. The static deflection of the non-moving foundation next to the lever was evaluated in order to eliminate drifts of the whole device or the chamber beneath the microscope. The evaluation algorithm to quantify the displacements interpolates between single pixels, leading to a sub-pixel resolution and an estimated overall displacement resolution of 0.1 μm.

The actuator reacts very quick (below the temporal resolution of the camera system, 100 fps) to temperature changes and the response time is rather determined by the Peltier-element itself. Assuming a Si-substrate volume of $8 \times 8 \times 0.4$ mm^3, the heat capacity of the device is about $C = 40$ mJ/K. For comparison, the Peltier-element can deliver 51.6 W of power and, therefore, can change the temperature of the test device about 1 K within 800 μs.

B. Out-of-Plane Deflection

A digital holographic microscope (DHM, LynceeTec) is used to quantify the out-of-plane deflection (*z*-direction) of the device. Again, the test-specimen is located on a temperature

controlled surface (Peltier-element + temperature control unit) and the topography is measured at a set of temperatures, especially the *z*-deflection of the tip of the lever. The measured out-of-plane deflection due to a temperature change from +9 °C up to +50 °C is only $d_z = 100$ nm. This deflection is small compared to the initial static deflection of 1.9 μm that occurs due to the intrinsic stress gradient within the structure's height, published in a previous work [24].

VII. RESULTS

A. Analytical Model and Design

The analytically calculated deformations of the V-shaped beam and the lever transmission are compared to simple Euler beams, modeled in a FEM simulation to verify the analytical model. The analytic spring stiffnesses (Eq. 1, Eq. 2) and the simulated ones are in excellent agreement to each other: $k_{L,ana} = 167.48$ N/m, $k_{L,FEM} = 167.52$ N/m and $k_{V,ana} = 33.02$ N/m, $k_{V,FEM} = 33.10$ N/m. Hence, it can be assumed that the simplifications applied in the analytic model are justified.

A closer look at the analytical model reveals that the energy losses due to the lever transmission and the deformation of the designed V-shaped beams are insignificant. The total deflection is primary defined by thermal expansion of the beams and the resulting amplification due to the V-shaped geometry. Due to the design, the terms including the composed spring stiffnesses in the denominator in Eq. 9 are small compared to $\sin(\gamma)$ and, hence, the energy losses due to the deformation of the structure are negligible. Furthermore, the Young's modulus E and the height h of the structure have no impact on the deflection. The relevant parameters for the blocking force can be approximated and summarized to be: $n \cdot A_2 \cdot \sin(\gamma) \frac{l_4}{h_L} \cdot E\alpha\Delta T$.

The blocking force times the deflection of the tip is a measure for the work W_{act} that the actuator can provide. Combining Eq. 3, Eq. 9, Eq. 10, and Eq. 11 and applying a rough approximation $(\sin(\gamma) \gg \frac{2l_0}{E \cdot A_2} k_{comp}, x_h(y_d) \sim \frac{1}{l_4} \cdot y_d \cdot h_L$, Taylor approximation up to $\mathcal{O}\{(\alpha\Delta T)^3\})$ leads to

$$W_{act} = 2 \cdot \underbrace{l_0 n A_2}_{\text{Geometry}} \cdot \underbrace{E(\alpha\Delta T)^2}_{\text{Material}}. \quad (12)$$

The most relevant parameters in Eq. 12 are again the Young's modulus and the squared product of the CTE and the temperature difference. The force and, therefore, also the maximum work of the actuator increases in direct proportion to the number of parallel V-shaped beams n, their cross section area A_2, and the V-shaped beam length l_0.

The analytical model can be extended for more complex geometries, by simply adding the spring stiffness k_{add} of the additional parts. The elastic energy of those parts can be added to the total energy in Eq. 5, as long as they are linked directly to the deflection of the V-shaped beam stack. Hence, the spring stiffness can be added to the composed spring stiffness, modified by the number of parallel V-shaped beams

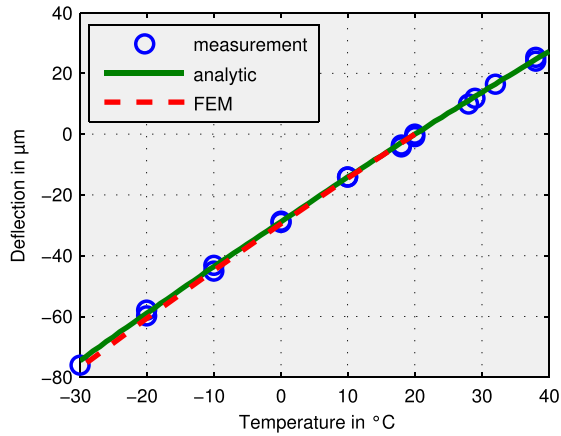$$\tilde{k}_{comp} = k_{comp} + \frac{k_{add}}{2n}. \quad (13)$$

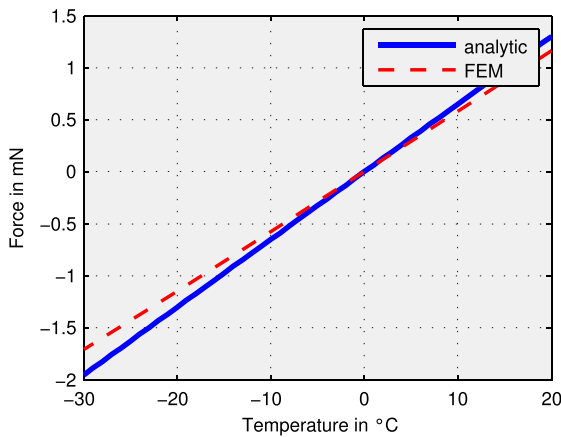Fig. 7. Measured deflection of the tip of the structure compared to the calculated and simulated ones.

Fig. 8. Analytically calculated and numerically simulated blocking force of the structure at different temperatures.

In this way, the analytical model of the V-shaped beam can easily be taken and adjusted to calculate other and more complex geometries.

B. Actuator Performance

The deflection at the tip of the fabricated structure is measured at different temperatures and compared to the analytical model, as well as to the results of the FEM simulation (Fig. 7). The FEM simulation as well as the analytical model are within a deviation of 1.5% in very good agreement to the measured deflections, even when the analytical model includes some approximations. The effective CTE in the simulations is set to $\alpha_{eff} = 11$ ppm [26]. Adding the CTE of the Si-substrate ($\alpha_{Si} = 2.6$ ppm) leads to a CTE of the plated Ni of $\alpha_{Ni} = 13.6$ ppm, which is in good agreement with the values of the CTE of bulk material ($\alpha_{Ni,bulk} = 13.4$ ppm, [27]). The presented thermal actuator exhibits a linear deflection coefficient of 1.48 μm/K, a simulated blocking force of 57 μN/K (Fig. 8), and occupies an area of 2135×1831 μm^2.

The in-plane spring constant of the actuator, regarding the displacement and force at the tip is $k_{in} = 38.5$ N/m. This value is calculated from the measured thermal characteristics of the
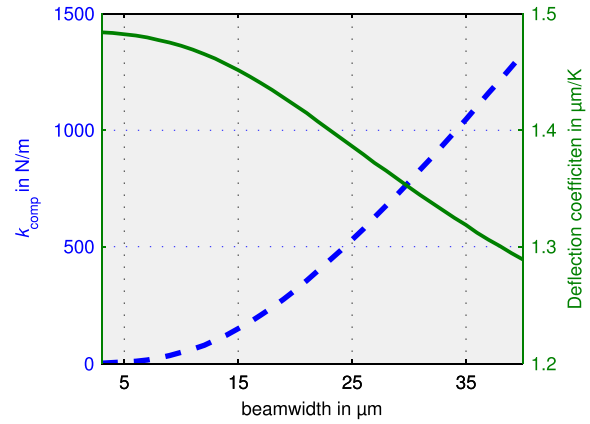

Fig. 9. Composed spring stiffness and deflection coefficient of the actuator at different minimal beam widths and a fixed aspect ratio.

actuator and verified by the FEM model. The corresponding out-of-plane stiffness is simulated to be only $k_{out} = 0.95$ N/m. For reliable operation, an out-of plane movement of the tip has to be restricted to avoid possible buckling in this direction. This can be achieved for instance by a top and bottom guidance when the actuator is packaged. Nevertheless, no significant out-of-plane deflection was observed in the presented design since the thermal expansion leads only to in-plane stress and no out-of-plane forces occur. Even though, the aspect ratio (height/width) of the Ni-structures should be as high as possible since the ratio of the in- and out-of-plane spring constants is proportional to h^2. It is technologically limited by the minimal feature size which is mainly defined by the hinges b_1 and the width of the coupling bars b_3. They have to be sufficiently small, so that $\sin(\gamma) \gg \frac{2l_0}{E \cdot A_2} k_{comp}$ (compare Eq. 9). Figure 9 depicts k_{comp} at different minimal beam widths, where $b_1 = b_3$. In addition, the coefficient of the deflection is plotted. For small minimal feature sizes (beam widths) the deflection becomes constant. When the beam width increases, the deflection drops due to the increasing deformation energy which acts as energy loss.

C. Temperature Threshold Sensor

For the proof-of-concept, the actuator is combined with a bistable switch to establish a passive temperature threshold sensor. Such a sensor allows for the tracking of proper storage and transportation temperatures of cooling goods, e.g., refrigerator cargo or blood bottles. The bistable beam switch is described in detail in [28] and [29]. It exhibits a total length of $l_{bb} = 2600$ μm, an effective apex height of $h_a = 33$ μm, a beam width of $t = 7$ μm, and is manufactured with the same process as the actuator. Two latching mechanisms are attached to the actuator and the bistable beam (Fig. 10). At first, the temperature is decreased until a well defined activation temperature is reached, where the first latch is activated. When the temperature is increased afterwards, the actuator pushes against the bistable beam until an upper threshold temperature is reached. At this temperature, the bistable beam switches into its second stable position and an irreversible contact is established with the second
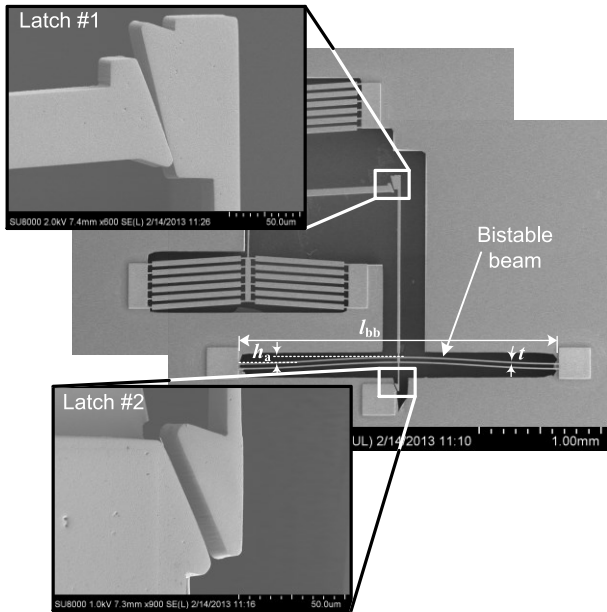
Fig. 10. Electron microscope micrograph of the established passive temperature threshold sensor. The thermal actuator is combined with a bistable beam and two latching mechanisms. The first one allows to activate the device at a well defined activation temperature and the second latch establishes an irreversible contact when an upper threshold temperature is reached.
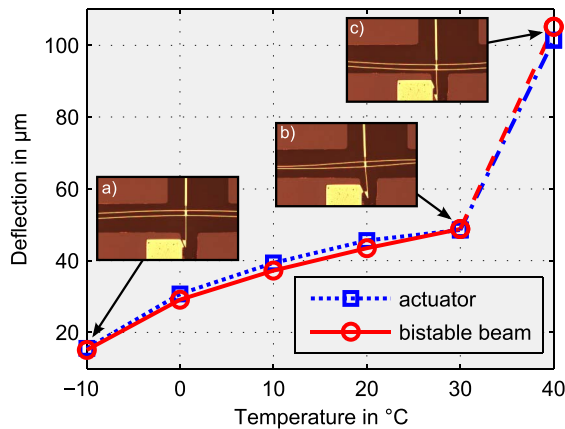

Fig. 11. The deflection of the actuator and the bistable beam, after the initial activation at -10 °C. The device is heated up until the bistable beam switches into its second stable position at $+30$ °C. The inserts depict microscope images of the bistable beam in a) its initial position, b) next to the switching point, and c) after the switching.

latching mechanism. A deflection of at least $d_{min} = 44$ μm and a peak force of $f_{max} = 100$ μN is required to push the bistable beam into its second stable position, where the available temperature change is only in the order of several 10 K. Hence, a thermal actuator featuring a high thermal sensitivity is required. Fig. 11 depicts the measured deflection of the tip of the lever and the bistable beam during the heat-up of the described threshold sensor, after the initial cool-down to activate the first latch mechanism. The deflection follows a non-linear curve, since the bistable beam exhibits a non-linear force-deflection curve. In addition the friction force of the latch #2 has to be overcome. The bistable beam snaps into its second stable position between $+30$ °C and $+40$ °C, which can be tuned by the design.

	μm/K	μN/K	mm^2	μJ/K^2/m^2
Steiner [26]	0.50	66	1.8	18.3
Sigmund [30], [31]	0.04	85	0.1	34.0
Qiu [32]	0.55	60	1.6	20.6
Khazaai [33]	0.48	14	1.3	5.2
This work	**1.48**	57	3.9	21.6

VIII. CONCLUSION

A completely passive thermal actuator is presented which exhibits an efficient conversion of the thermally induced elastic energy into mechanical work. It relies only on the temperature of the surrounding environment, where the device exhibits a quasi-static homogenous temperature distribution. The actuator is made of electroplated Ni on a Si-substrate with wafer level state of the art micro-fabrication technologies. An analytical model is set up and numerical simulations are carried out to design and predict the characteristics of the actuator. Both are in good agreement to each other and to the measured deflections of the manufactured structures. The models are also exploited to calculate the blocking force that the actuator can provide at a specific temperature difference. Furthermore, the analytical model reveals the most relevant parameters for the work such actuators can do: The Young's modulus E, the squared product of $\alpha \cdot \Delta T$, as well as the length, number, and area of the V-shaped beams. It can be extended to more complex actuator geometries that rely on V-shaped beams by adding the deformation energy of the additional parts to the total energy.

The investigated actuator achieves a temperature dependent deflection of 1.48 μm/K, a simulated blocking force of 57 μN/K, and occupies a total area of 2135×1831 μm^2. The actuator exhibits and outstanding temperature dependent deflection passing state of the art actuators by a factor of three. Table III summarizes the performances of the most relevant state of the art actuators and compares them to the presented design. The area specific work (force-displacement product) is calculated to be 21.7 μJ/K^2 /m^2 for the presented actuator. In principle, the thermally induced elastic energy can be converted relatively lossless into a mechanical force. Hence, the actuator presented in [30] and [31] exhibits the highest area specific work of all compared state of the art actuators. Trading off this force into more displacement results in elastic deformation losses that increase with larger deflections. Due to the design of the presented actuator, the energy losses caused by the deformation of the structure have been drastically reduced. Hence, its area specific work is competitive to state of the art actuators, but offers much more displacement per Kelvin. The actuator is designed for a maximal temperature range of -50 °C up to $+100$ °C. For higher/lower temperatures, the yield strength of the material will be exceeded in the most stressed parts of the actuator. This leads to plastic deformations and a non-linear and unreproducible behavior.

Furthermore, a completely passive temperature threshold sensor is established as proof-of-concept where a bistable

beam is switched between two stable positions, only with the thermal energy of the surrounding ambient.

REFERENCES

[1] N.-T. Nguyen, S.-S. Ho, and C. L.-N. Low, "A polymeric microgripper with integrated thermal actuators," *J. Micromech. Microeng.*, vol. 14, no. 7, pp. 969–974, Jul. 2004.

[2] J. J. Khazaai, M. Haris, H. Qu, and J. Slicker, "Displacment amplification and latching mechanism using V-shape actuators in design of electro-thermal MEMS switches," in *Proc. IEEE Sensors*, Nov. 2010, pp. 1454–1459.

[3] G.-K. Lau, J. F. L. Goosen, F. van Keulen, T. C. Duc, and P. M. Sarro, "Polymeric thermal microactuator with embedded silicon skeleton: Part I—Design and analysis," *J. Microelectromech. Syst.*, vol. 17, no. 4, pp. 809–822, Aug. 2008.

[4] T. C. Duc, G.-K. Lau, and P. M. Sarro, "Polymeric thermal microactuator with embedded silicon skeleton: Part II—Fabrication, characterization, and application for 2-DOF microgripper," *J. Microelectromech. Syst.*, vol. 17, no. 4, pp. 823–831, Aug. 2008.

[5] J. Wei, T. C. Duc, and P. M. Sarro, "An electro-thermal silicon-polymer micro-gripper for simultaneous in-plane and out-of-plane motions," in *Proc. Eurosensors*, 2008, pp. 7–10.

[6] A. Unamuno, R. Blue, and D. Uttamchandani, "Modeling and characterization of a vernier latching MEMS variable optical attenuator," *J. Microelectromech. Syst.*, vol. 22, no. 5, pp. 1229–1241, Oct. 2013.

[7] C. Guan and Y. Zhu, "An electrothermal microactuator with Z-shaped beams," *J. Micromech. Microeng.*, vol. 20, no. 8, p. 085014, Aug. 2010.

[8] M. Daneshmand, S. Fouladi, R. R. Mansour, M. Lisi, and T. Stajcer, "Thermally actuated latching RF MEMS switch and its characteristics," *IEEE Trans. Microw. Theory Techn.*, vol. 57, no. 12, pp. 3229–3238, Dec. 2009.

[9] A. A. Geisberger, N. Sarkar, M. Ellis, and G. D. Skidmore, "Electrothermal properties and modeling of polysilicon microthermal actuators," *J. Microelectromech. Syst.*, vol. 12, no. 4, pp. 513–523, Aug. 2003.

[10] Q.-A. Huang and N. K. S. Lee, "Analysis and design of polysilicon thermal flexure actuator," *J. Micromech. Microeng.*, vol. 9, no. 1, p. 64, 1999.

[11] G. Vitellaro, G. L'Episcopo, C. Trigona, B. Ando, and S. Baglio, "A compliant MEMS device for out-of-plane displacements with thermo-electric actuation," *J. Microelectromech. Syst.*, vol. 23, no. 3, pp. 661–671, Jun. 2014.

[12] J.-S. Park, L. L. Chu, A. D. Oliver, and Y. B. Gianchandani, "Bent-beam electrothermal actuators—Part II: Linear and rotary microengines," *J. Microelectromech. Syst.*, vol. 10, no. 2, pp. 255–262, Jun. 2001.

[13] L. Que, J.-S. Park, and Y. B. Gianchandani, "Bent-beam electrothermal actuators—Part I: Single beam and cascaded devices," *J. Microelectromech. Syst.*, vol. 10, no. 2, pp. 247–254, Jun. 2001.

[14] C. Lee and C.-Y. Wu, "Study of electrothermal V-beam actuators and latched mechanism for optical switch," *J. Micromech. Microeng.*, vol. 15, no. 1, pp. 11–19, Jan. 2005.

[15] Y. Zhu, A. Corigliano, and H. D. Espinosa, "A thermal actuator for nanoscale *in situ* microscopy testing: Design and characterization," *J. Micromech. Microeng.*, vol. 16, no. 2, pp. 242–253, Feb. 2006.

[16] M. D. Williams, F. van Keulen, and M. Sheplak, "Modeling of initially curved beam structures for design of multistable MEMS," *J. Appl. Mech.*, vol. 79, no. 1, p. 011006, 2012.

[17] J. Zhao, J. Jia, X. He, and H. Wang, "Post-buckling and snap-through behavior of inclined slender beams," *J. Appl. Mech.*, vol. 75, no. 4, p. 041020, 2008.

[18] J. J. Khazaai and H. Qu, "Electro-thermal MEMS switch with latching mechanism: Design and characterization," *IEEE Sensors J.*, vol. 12, no. 9, pp. 2830–2838, Sep. 2012.

[19] B. Ando, S. Baglio, N. Savalli, and C. Trigona, "Cascaded 'triple-bent-beam' MEMS sensor for contactless temperature measurements in nonaccessible environments," *IEEE Trans. Instrum. Meas.*, vol. 60, no. 4, pp. 1348–1357, Apr. 2011.

[20] J. W. Wittwer, M. S. Baker, and L. L. Howell, "Simulation, measurement, and asymmetric buckling of thermal microactuators," *Sens. Actuators A, Phys.*, vol. 128, no. 2, pp. 395–401, Apr. 2006.

[21] E. T. Enikov, S. S. Kedar, and K. V. Lazarov, "Analytical model for analysis and design of V-shaped thermal microactuators," *J. Microelectromech. Syst.*, vol. 14, no. 4, pp. 788–798, Aug. 2005.

[22] J. R. Allegra, J. Brennan, V. Lanier, R. Lavery, and B. MacKenzie, "Storage temperatures of out-of-hospital medications," *Academic Emergency Med.*, vol. 6, no. 11, pp. 1098–1103, Nov. 1999.

[23] L. H. Brown, K. Krumperman, and C. J. Fullagar, "Out-of-hospital medication storage temperatures: A review of the literature and directions for the future," *Prehospital Emergency Care*, vol. 8, no. 2, pp. 200–206, Jan. 2004.

[24] W. E. G. Hansal *et al.*, "Microgalvanic nickel pulse plating process for the fabrication of thermal microactuators," *Microsyst. Technol.*, vol. 20, nos. 4–5, pp. 681–689, Apr. 2014.

[25] S. He, J. S. Chang, L. Li, and H. Ho, "Characterization of Young's modulus and residual stress gradient of MetalMUMPs electroplated nickel film," *Sens. Actuators A, Phys.*, vol. 154, no. 1, pp. 149–156, Aug. 2009.

[26] H. Steiner, W. Hortschitz, M. Stifter, F. Keplinger, and T. Sauter, "Thermal actuators featuring large displacements for passive temperature sensing," *Microsyst. Technol.*, vol. 20, nos. 4–5, pp. 551–557, Apr. 2014.

[27] D. R. Lide, *CRC Handbook of Chemistry and Physics: A Ready-Reference Book of Chemical and Physical Data 2008–2009*. Boca Raton, FL, USA: CRC Press, 2008, doi: 10.1109/MESS.2014.7010249.

[28] H. Steiner, W. Hortschitz, M. Stifter, and F. Keplinger, "Thermal actuated passive bistable MEMS switch," in *Proc. Microelectron. Syst. Symp. (MESS)*, May 2014, pp. 1–5.

[29] J. Qiu, J. H. Lang, and A. H. Slocum, "A curved-beam bistable mechanism," *J. Microelectromech. Syst.*, vol. 13, no. 2, pp. 137–146, Apr. 2004.

[30] O. Sigmund, "Design of multiphysics actuators using topology optimization—Part II: Two-material structures," *Comput. Methods Appl. Mech. Eng.*, vol. 190, nos. 49–50, pp. 6605–6627, Oct. 2001.

[31] O. Sigmund, "Design of multiphysics actuators using topology optimization—Part I: One-material structures," *Comput. Methods Appl. Mech. Eng.*, vol. 190, nos. 49–50, pp. 6577–6604, Oct. 2001.

[32] J. Qiu, J. H. Lang, A. H. Slocum, and A. C. Weber, "A bulk-micromachined bistable relay with U-shaped thermal actuators," *J. Microelectromech. Syst.*, vol. 14, no. 5, pp. 1099–1109, Oct. 2005.

[33] J. J. Khazaai, H. Qu, M. Shillor, and L. Smith, "Design and fabrication of electro-thermally activated micro gripper with large tip opening and holding force," in *Proc. IEEE Sensors*, Oct. 2011, pp. 1445–1448.

Authors' photographs and biographies not available at the time of publication.